JACS
JOURNAL OF THE AMERICAN CHEMICAL SOCIETY
Article
pubs.acs.org/JACS

Silica Nanopollens Enhance Adhesion for Long-Term Bacterial Inhibition

Hao Song,[†] Yusilawati Ahmad Nor,[†] Meihua Yu,[†] Yannan Yang,[†] Jun Zhang,[†] Hongwei Zhang,[†] Chun Xu,[†] Neena Mitter,[‡] and Chengzhong Yu*[,†]

[†]Australian Institute for Bioengineering and Nanotechnology, The University of Queensland, Brisbane 4072, Australia
[‡]Queensland Alliance for Agriculture and Food Innovation, The University of Queensland, Brisbane 4072, Australia

Supporting Information

ABSTRACT: Nature's creations with spiky topological features typically exhibit intriguing surface adhesive properties. From micrometer-sized pollen grains that can easily stick to hairy insects for pollination to nanoscale virus particles that are highly infectious toward host cells, multivalent interactions are formed taking advantage of rough surfaces. Herein, this nature-inspired concept is employed to develop novel drug delivery nanocarriers for antimicrobial applications. A facile new approach is developed to fabricate silica nanopollens (mesoporous silica nanospheres with rough surfaces), which show enhanced adhesion toward bacteria surfaces compared to their counterparts with smooth surfaces. Lysozyme, a natural antimicrobial enzyme, is loaded into silica nanopollens and shows sustained release behavior, potent antimicrobial activity, and long-term total bacterial inhibition up to 3 days toward *Escherichia coli*. The potent antibacterial activity of lysozyme-loaded silica nanopollens is further demonstrated *ex vivo* by using a small-intestine infection model. Our strategy provides a novel pathway in the rational design of nanocarriers for efficient drug delivery.

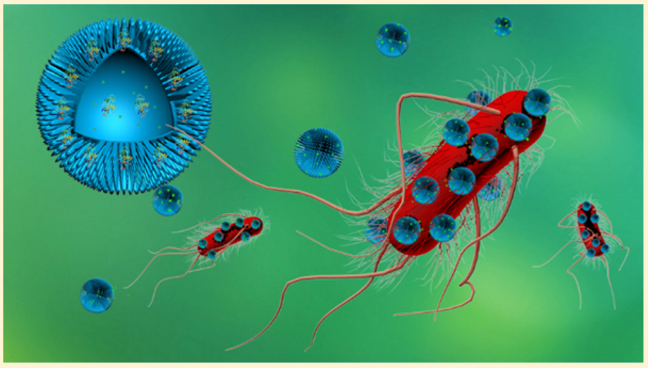

INTRODUCTION

Intriguing natural systems have inspired remarkable advances in the development of functional materials with versatile applications.[1−4] Pollen grains with distinct rough surfaces are extraordinary delivery vectors in nature. With a large inner cavity for encapsulating genetic materials, pollen particles exhibit nanoscale channels as well as numerous spikes on the outer shell (extine),[5,6] enabling adhesion toward hairy insect legs and mouthparts for easy pollination.[7] Apart from micrometer-sized pollens, some viruses, with dimensions ranging from 30 to 400 nm, also show rough topologies.[8] The surface spikes form multiple "entry claws" that bind to the cell membrane during virus invasion,[9] which multiplies the receptor-specific interaction and leads to high viral infectivity. Indeed, surface-roughness-enhanced adhesion via multivalent interactions has been observed at various length scales and applied in daily life.[10] However, limited progress has been made using this nature-derived principle to engineer nanoparticles for various drug delivery applications.[11−14]

Bacterial infection continues to present a major threat to public health, especially with increasing levels of antimicrobial resistance in recent decades.[15,16] Lysozyme is a natural antimicrobial protein that catalyzes the hydrolysis of peptidoglycan in bacterial cell walls.[17] Unfortunately, lysozyme is insensitive to most Gram-negative strains, such as *Escherichia coli* (*E. coli*),[18] and its instability further hinders its widespread application.[19−22] To tackle these problems, extensive efforts have been devoted to develop various nanomaterials, including polymers,[23] nanomotors,[19] ZnO,[21] and silica nanoparticles,[24−28] to immobilize lysozyme and improve the antimicrobial performance. Notably, in the current nanoparticle-based formulations, lysozyme is typically coated on the nanoparticle's outer surface to affiliate a positive surface charge and enhance the interaction toward the bacterial cell wall via electrostatic attraction.[24,25] However, the exposure of lysozyme on the external surface increases the chance of denaturation,[27] which is not favorable for long-term antibacterial activity. It is a challenge to design novel nanocarriers for long-term bacterial inhibition, especially toward *E. coli*.

The surface of bacteria is generally covered with a range of pili 5−8 nm in diameter and several micrometers in length.[29] Similar to the rough pollen particles which can easily adhere on the hairy legs of a honey bee,[7] nanocarriers mimicking pollen structures are hypothesized to have enhanced adhesion toward the "hairy" bacterial surface and thus improved lysozyme delivery efficacy. Surface roughness of biomaterials has been widely recognized as a key feature that influences the surface−bacteria interactions,[30] and nanoscale roughness engineered on titanium surface has shown enhanced bacterial attachment.[31,32]

Received: January 8, 2016
Published: May 3, 2016

DOI: 10.1021/jacs.6b00243
J. Am. Chem. Soc. 2016, 138, 6455−6462

The synthesis of mesoporous silica nanoparticles with rough surface was reported only recently,[13,14] where multiple steps including complicated surface modifications are required to generate surface roughness and surfactants are needed to template the mesopores in the silica wall.[13,33] For practical use in antibacterial applications, scalable and cheap synthesis of nanocarriers with excellent performance is highly desired. Moreover, there is no report on the influence of surface topology of nanocarriers on their adhesive properties on bacteria surface and lysozyme delivery performance.

Herein, for the first time, we report the synthesis of silica nanopollens—i.e., rough mesoporous silica hollow spheres (R-MSHSs)—through a one-pot, surfactant-free, cheap, and scalable approach. As shown in Scheme 1, by simply introducing resorcinol (R), formaldehyde (F), and tetraethyl orthosilicate (TEOS) into a typical Stöber synthesis solution, RF@RF-SiO_2@RF (Scheme 1a, I) nanocomposites are assembled by selectively forming a RF core first, followed by the co-condensation of silica and RF interpenetrating shell. After calcination, R-MSHSs (Scheme 1a, II) with accessible inner cavity and spiky surface are obtained. The morphology of R-MSHSs is similar to that of pollen grains,[34] while the size is smaller (thus they are named as silica nanopollens). It is demonstrated that silica nanopollens show enhanced adhesion toward bacterial surfaces (Scheme 1b). The silica nanopollens loaded with lysozyme exhibit a sustained release profile and potent antimicrobial activity toward *E. coli*, achieving a total bacterial inhibition in a duration of 3 days.

Scheme 1. Silica Nanopollens for Efficient Antibacterial Treatment: (a) Schematic Illustration of the Synthesis of Silica Nanopollens and (b) Efficient Lysozyme Delivery via Silica Nanopollens Which Are Adhesive toward Bacterial Surfaces (Size Not to Scale)

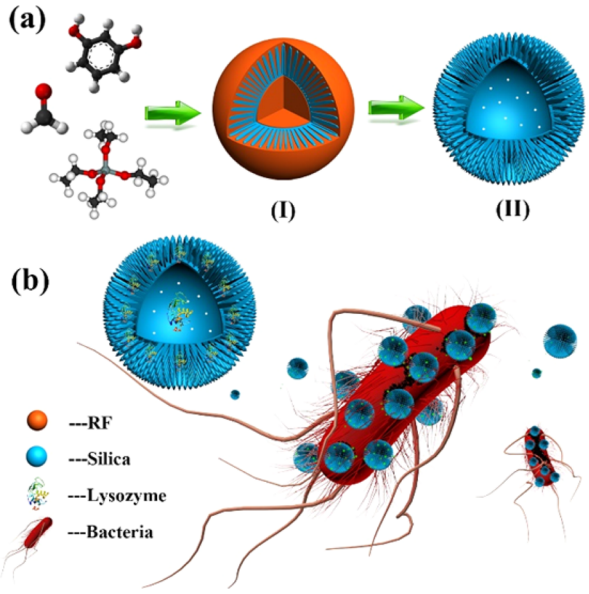

RESULTS AND DISCUSSION

Transmission electron microscopy (TEM) shows that well-dispersed silica nanopollens with a uniform and exclusive hollow morphology are obtained (Figure 1a). The mean particle diameter is measured to be 256 ± 17 nm. At a higher magnification (Figure 1b), it is clear that each silica nanopollen has an inner hollow cavity (165 nm in diameter) and a shell (52 nm in thickness) covered with nanosized silica spikes, similar to the morphology of pollen particles.[34] Dynamic light scattering (DLS) results (Figure S1) further confirm that the nanospheres are monodispersed, with a polydispersity index (PDI) of 0.1. The hydrodynamic particle size is measured to be 295 nm, which is slightly larger than the size obtained in TEM images due to the hydration of silica by surrounding water.[35]

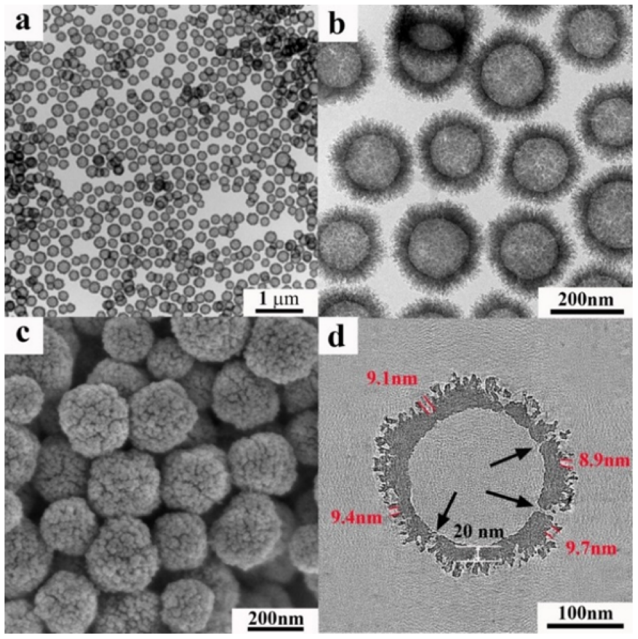

Figure 1. (a,b) TEM images, (c) SEM image, and (d) ET slice of rough mesoporous silica hollow spheres (R-MSHSs).

Scanning electron microscopy (SEM) image further shows the nanoscale surface roughness with a dense distribution of silica spikes on the surface (Figure 1c). To investigate whether the hollow cavity of silica nanopollen is accessible, electron tomography (ET)[36,37] was used to further explore the detailed structure. The tomogram sliced from the center of one particle (Figure 1d) clearly presents a hollow cavity with a diameter of 175 nm and the spiky silica shell with a thickness of 45 nm. The shell consists of two parts: (1) a relatively dense silica layer with a thickness of around 20 nm and (2) a 25-nm-thick porous layer composed of nanospikes (average diameter of 5 nm) grown on the first layer. The distance between two adjacent nanospikes measured from the ET slice is around 9 nm. Similar to the pollen grains with nanoscale channels on the extine,[5] there exist several channels (Figure 1d, shown with black arrows) with a diameter around 2−4 nm distributed in the dense silica shell connecting the inner hollow space with the outer atmosphere. The distribution of more nanochannels in the nanosphere can be seen evidently from the tomogram movie in the SI.

To characterize the porous nature of silica nanopollens, nitrogen sorption analysis was conducted. The nitrogen adsorption and desorption isotherm (Figure S2a) shows a typical type IV isotherm with a major capillary condensation step at a relative pressure (P/P_0) around 0.8. The corresponding Barrett−Joyner−Halenda (BJH) pore size distribution curve (Figure S2b) derived from the adsorption branch exhibits a relatively broad peak centered at 9.3 nm, in accordance with the distance between two adjacent spikes measured from the ET slice (~9 nm). The Brunauer−

DOI: 10.1021/jacs.6b00243
J. Am. Chem. Soc. 2016, 138, 6455−6462

Emmett−Teller (BET) surface area and the total pore volume of R-MSHSs are 183 $m^2 \cdot g^{-1}$ and 0.37 $cm^3 \cdot g^{-1}$, respectively.

The structures of silica nanospheres can be easily tuned by adjusting silica precursor amount. Typically, resorcinol and formaldehyde were first introduced into the synthesis system forming RF Stöber nanospheres,[38] then 0.6 mL of TEOS was added followed with the second addition of RF precursors to fabricate R-MSHSs (see experimental details in Supporting Information). By increasing the TEOS amount to 1.4 mL, uniform and dispersed rough nanospheres can be obtained with relatively dense silica shell (Figure 2a). ET result (Figure 2b)

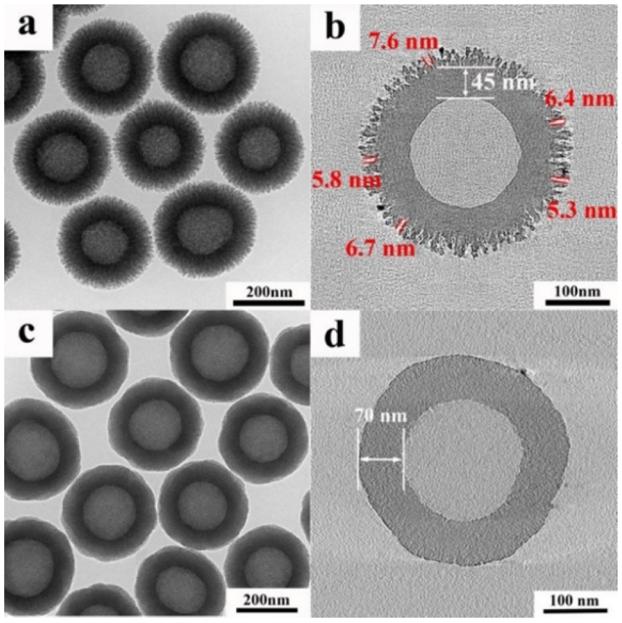

Figure 2. TEM images (a,c) and corresponding ET slices (b,d) of rough mesoporous silica hollow spheres with blocked shell (R-MSHSs-B) (a,b) and smooth silica hollow spheres (S-SHSs) (c,d).

shows that there exists a dense silica layer (~45 nm in thickness) beneath the silica spikes, which blocks the inner cavity being accessible. For this reason, this particle is named as R-MSHSs-B hereafter. The distance between two adjacent spikes estimated from the ET slice is around 6 nm, smaller than that of R-MSHSs. By decreasing the TEOS amount from 0.6 to 0.4 mL, rough mesoporous silica hollow spheres with collapsed shell (R-MSHSs-C) were obtained (Figure S3), since limited silica source results in incomplete silica coverage rending the shell to be fragile and easily collapsed during high temperature calcination.

The second addition of resorcinol and formaldehyde together with TEOS is important for the formation of surface spikes. By adding only TEOS at this stage, smooth silica hollow spheres (S-SHSs) were obtained with a uniform silica shell of 73 nm (Figure 2c). The ET result (Figure 2d) shows that the 70-nm-thick silica shell is dense and the outer surface is relatively smooth, without any silica spikes. The porosity of silica hollow spheres prepared at different conditions was also characterized by nitrogen sorption analysis (Figure S4a). S-SHSs possess a low surface area of 57 $m^2 \cdot g^{-1}$ and pore volume of 0.06 $cm^3 \cdot g^{-1}$, with no obvious mesopores identified in the shell (Table S1, Figure S4b). The pore size of R-MSHSs-B is distributed around 6.3 nm, in accordance with the ET results. The broad pore size distribution of R-MSHSs-C (10−40 nm) may be attributed to the enlarged porous space between spikes as well as collapsed hollow cavities.

The formation mechanism of silica nanopollens was further investigated. It should be noted that the disappearance of spiky nanostructures on silica hollow spheres without a second addition of RF precursors indicates that the co-condensation of resorcinol and formaldehyde together with silica species is the key to form surface spikes. To gain a detailed understanding of the co-condensation process, a time-dependent study was conducted during the synthesis of R-MSHSs and R-MSHSs-B. RF nanospheres with diameters around 180 nm (Figure S5i, RF, see also schematic illustration in Figure S5ii) were obtained 6 h after the first addition of resorcinol and formaldehyde. To fabricate R-MSHSs, 0.6 mL of TEOS, 0.4 g of resorcinol, and 0.56 mL of formaldehyde were introduced in the second addition. Due to the slow polymerization behavior of RF,[39] silica species first hydrolyzed and heterogeneously nucleated on the RF nanosphere surface within 5 min (Figure S5i,ii, a1). The limited amount of silicate nuclei resulted in an incomplete coverage of the RF nanosphere surface. This is further confirmed by TEM of samples after calcination, where separate silica nanoparticles (~10−15 nm) are observed (inset of Figure S5i, a1). When the time was prolonged to 30 min, silica nuclei, after growth, merged into a relatively dense layer, but some crevices connecting the hollow space could still be observed in the calcined sample (Figure S5i,ii, b1). The spiky surface emerges at the reaction time of 1 h, when RF species start to nucleate (Figures S5i,ii, c1).[39] The further growth of silica within the silica/RF matrix is restricted by the surrounding RF framework, resulting in radial growth of silica spikes. R-MSHSs with obvious spiky morphology can be obtained after 2 h of reaction (Figure S5i,ii, d1).

For the synthesis of R-MSHSs-B, increasing the amount of TEOS to 1.4 mL results in a relatively faster silica condensation rate, leading to a uniform and intact silica layer coated on RF nanospheres within 5 min (Figures S5i,ii, a2). The inner cavity is evidently blocked by a dense silica shell with a thickness of 40 nm (Figures S5i,ii, b2) when the reaction time reaches 30 min. Further co-condensation of RF and silica species leads to the formation of surface spikes on R-MSHSs-B (Figures S5i,ii, c2 and d2). In contrast, when the TEOS amount was decreased to 0.4 mL, incomplete silica shell coverage toward the RF core rendered the nanoparticles fragile and easily collapsed.

By controlling the polymerization kinetics of this RF−silica system, tailored nanostructures can be achieved through a one-pot approach without the assistance of surfactants. The synthesis of silica nanopollens can be easily scaled up to a yield of 2.5 g in one batch (Figure S6). Moreover, the choice of cheap precursors is also favorable for practical applications. This facile synthesis approach enabled successful fabrication of silica hollow spheres with controllable surface roughness. In analogy to the adhesion of pollen toward hairy insect legs, it is hypothesized that the introduction of surface roughness will enhance the interaction of our nanopollens with bacterial surfaces. Thus, the bacterial adhesion property of these silica nanoparticles was further investigated.

E. coli, a typical Gram-negative bacteria, was incubated with silica hollow spheres (concentration of 100 $\mu g \cdot mL^{-1}$) in Luria broth (LB) medium. The particle−bacteria adhesion was directly observed under electron microscopy after bacteria fixation and staining. As shown in Figure 3a, *E. coli* exhibits intact rod-like morphology with fewer S-SHSs adhered on bacterial surface compared to R-MSHSs-B (Figure 3b) and R-

DOI: 10.1021/jacs.6b00243
J. Am. Chem. Soc. 2016, 138, 6455−6462

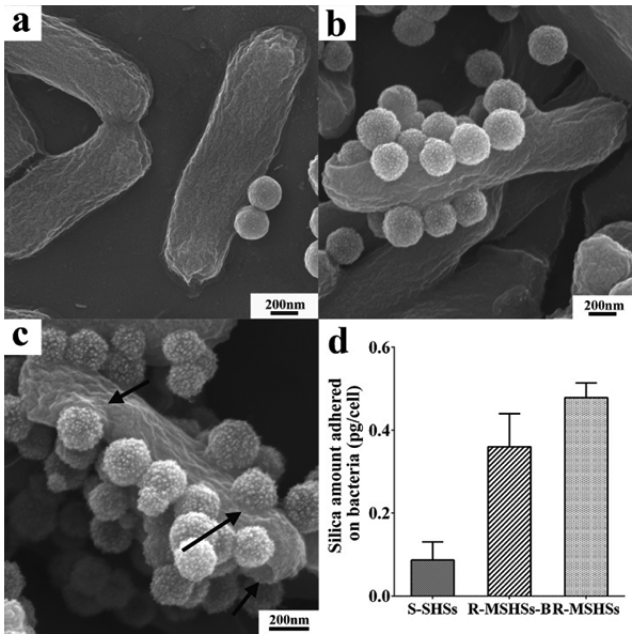

Figure 3. SEM images of (a) S-SHSs, (b) R-MSHSs-B, and (c) R-MSHSs adhered on *E. coli* surface. (d) Quantitative analysis of silica content adhered on bacteria from ICP-OES.

MSHSs (Figure 3c). Comparing with S-SHSs (Figure S7a), the increased particle number of both R-MSHSs-B (Figure S7b) and R-MSHSs (Figure S7c) adhered on bacterial surface is also confirmed by TEM results. Notably, some of the R-MSHSs are partially engulfed into the bacterial cell wall, leaving a semispherical dent on the bacterial surface upon detachment (Figure 3c, black arrows). The engulfment process is typically related to the strength of the attractive cell membrane−particle interactions,[40] an indication of enhanced adhesion between R-MSHSs and the bacterial cell wall. In contrast, the smooth surface of S-SHSs provides limited contact area for interfacial interaction,[41] resulting in fewer particles being adhered on the bacterial surface. Moreover, electrostatic repulsion between both negatively charged silica nanoparticles and bacteria surface hinders their interaction as well.[25] It is favorable to enhance the electrostatic attraction toward bacteria for silica nanoparticles by amine modification. However, the unwanted toxicity induced by the amine groups remains a concern.[42] Here, as a result of engineered surface roughness, both R-MSHSs-B and R-MSHSs show enhanced bacterial adhesion property, which may be attributed to the multivalent interactions induced by their surface spikes when contacting with the hairy bacteria surface, resulting in strong adhesion via a large number of contacts.[10]

To quantitatively analyze the amount of silica adhered on the bacteria surface, the micro-sized bacteria cultured with silica nanospheres were filtered through a 450-nm-pore filter membrane. Extensive washing was applied to remove the isolated particles from the solution. Bacteria-free samples were also analyzed as background to eliminate the interference from aggregated silica nanospheres. The inductively coupled plasma optical emission spectrometry (ICP-OES) results (Figure 3d) show that less than 0.1 pg of S-SHSs adhere on each bacteria surface, whereas 0.36 pg of R-MSHSs-B and 0.48 pg of R-

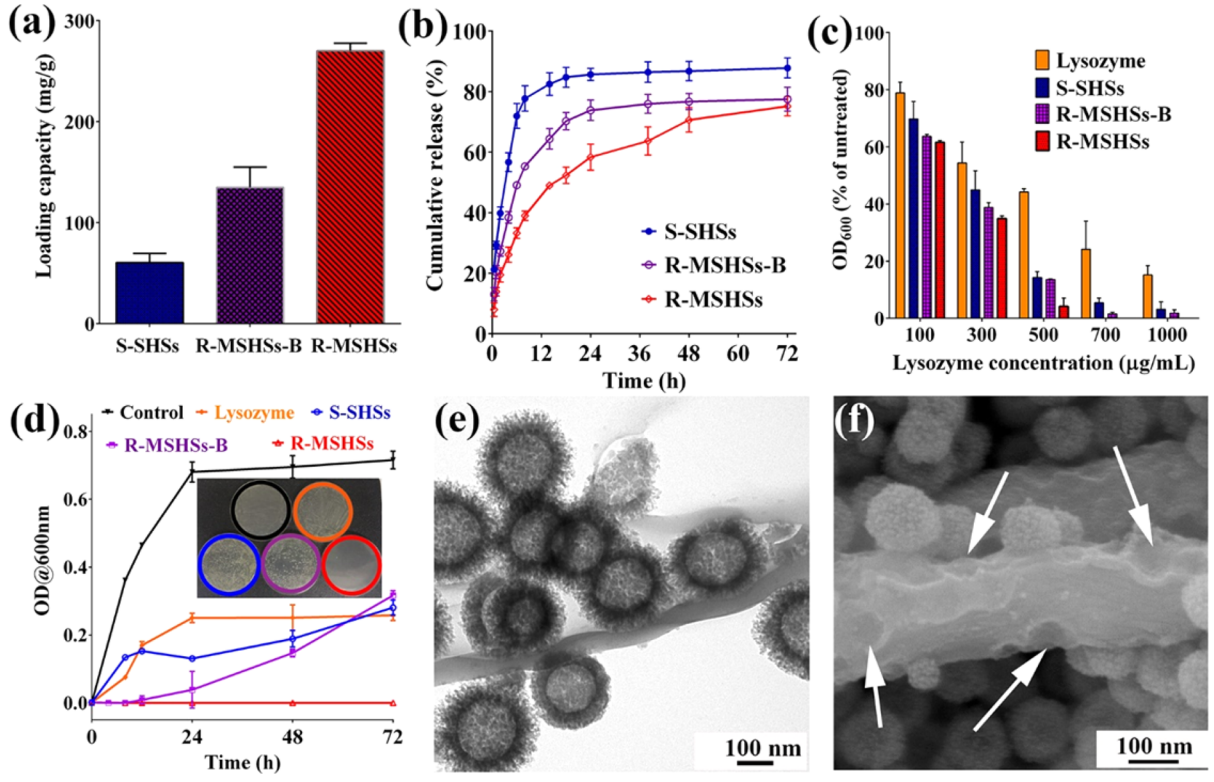

Figure 4. (a) Lysozyme loading and (b) release profile for S-SHSs, R-MSHSs-B, and R-MSHSs. (c) Dose-dependent antibacterial activities of free lysozyme and lysozyme-loaded nanospheres toward *E. coli* for 24 h. (d) Time-dependent antibacterial activities of free lysozyme and lysozyme-loaded silica nanospheres at the lysozyme dosage of 700 $\mu g \cdot mL^{-1}$. Inset: digital photography of agar plates spread with bacteria suspension after 3-day treatment. (e) TEM and (f) SEM images of *E. coli* treated with lysozyme-loaded R-MSHSs for 24 h.

DOI: 10.1021/jacs.6b00243
J. Am. Chem. Soc. 2016, 138, 6455−6462

MSHSs remain on each bacteria. To estimate the particle numbers adhered on bacteria surface, a simplified model is employed to roughly calculate the apparent density and weight of S-SHSs, R-MSHSs-B, and R-MSHSs (Figure S8). According to this calculation (Table S2), fewer than 4 S-SHSs remain on the bacteria, which is in accordance with the SEM/TEM results. In contrast, it is estimated that more than 14 R-MSHSs-B and 39 R-MSHSs adhere on the cell wall, which are in the range identified from TEM/SEM results (17−38 R-MSHSs-B per cell; 30−69 R-MSHSs per cell). Comparing to R-MSHSs-B, the increased number of R-MSHSs adhered on bacteria is presumably due to the lower apparent density (1.26 vs 1.45 $g{\cdot}cm^{-3}$) and larger pore size to entangle the pili on the bacteria surface.[29]

To identify whether these silica nanoparticles will influence the bacterial growth, a dose-dependent nanoparticle toxicity assay toward *E. coli* was conducted. The results (Figure S7d) indicate a slightly inhibited bacterial growth as the dosage of silica nanoparticles was increased (from 100 $\mu g{\cdot}mg^{-1}$ to 1 $mg{\cdot}mg^{-1}$). Comparing with the S-SHSs, rough nanoparticles, especially R-MSHSs, exhibit higher toxicity, resulting from the stronger interaction with the bacterial membrane. However, less than 20% of bacterial inhibition can be observed at concentrations up to 1 $mg{\cdot}mL^{-1}$ for R-MSHSs, which indicates that the nanospheres possess relatively low toxicity toward bacteria.

To demonstrate the efficiency of nanoparticles delivery, lysozyme as a natural antimicrobial enzyme was immobilized in these silica hollow spheres. As shown in Figure 4a, due to the limited external surface area provided for lysozyme adsorption, S-SHSs show the lowest loading capacity of only 61 $\mu g{\cdot}mg^{-1}$. In contrast, R-MSHSs exhibit the highest loading capacity of 270 $\mu g{\cdot}mg^{-1}$, which is 2 times that achieved by R-MSHSs-B (135 $\mu g{\cdot}mg^{-1}$). This is attributed to the increase of mesopore volume from 0.117 (R-MSHSs-B) to 0.229 (R-MSHSs) $cm^3{\cdot}g^{-1}$ (Table S1).[43] The surface zeta potential of silica hollow spheres before and after lysozyme loading (Figure S9) was characterized in 10 mM phosphate buffer solution (PBS). After lysozyme loading, the zeta potential of S-SHSs changes dramatically from −29 to −3 mV, indicating that the positively charged lysozyme is adsorbed on the external surface. However, for R-MSHSs-B and R-MSHSs, their surface charges change from −19 and −18 mV to −8 and −6 mV, respectively. This suggests that lysozyme molecules are typically immobilized in the mesopores of rough nanospheres, resulting in limited neutralization of surface charge.

Lysozyme release behavior from silica nanospheres (Figure 4b) was examined under conditions with a fixed initial lysozyme concentration (270 $\mu g{\cdot}mL^{-1}$) in PBS. S-SHSs exhibit a boost in the release of lysozyme, with more than 85% released within 18 h. Compared to the smooth particles, R-MSHSs-B show a relatively slower release rate, with around 75% of lysozyme released at 24 h. R-MSHSs exhibit the most sustained release profile among the three types of particles, with only 74% of lysozyme released at 72 h. However, R-MSHSs with a relatively large pore size are supposed to have a fast release profile.[26] The retarded release of protein molecules from R-MSHSs may result from the enhanced surface hydrophobicity induced by the surface roughness and accessible inner cavity.[13]

The *in vitro* antibacterial activity of free lysozyme and lysozyme-loaded silica nanospheres was evaluated by the optical density (OD) measurement. *E. coli* (5×10^6 $CFU{\cdot}mL^{-1}$) was incubated with various concentrations of lysozyme and corresponding lysozyme-loaded nanospheres for 24 h. Dose-dependent antibacterial performance is observed for all the samples (Figure 4c). Lysozyme-immobilized silica nanospheres show higher activity compared to free lysozyme at the same dosage, which is more significant at lysozyme concentrations higher than 500 $\mu g{\cdot}mL^{-1}$. Rough nanoparticles exhibit enhanced antibacterial activity toward *E. coli*, especially for R-MSHSs, showing a minimum inhibitory concentration (MIC) value of 700 $\mu g{\cdot}mL^{-1}$. In contrast, the MIC of free lysozyme toward *E. coli* cannot be achieved, even at a concentration as high as 2 $mg{\cdot}mL^{-1}$ (data not shown).

As shown in Figure 4c, the antibacterial activity of various lysozyme formulations has a sequence of R-MSHSs > R-MSHSs-B > S-SHSs consistently at all lysozyme concentrations, except the difference between R-MSHSs-B and S-SHSs is not significant at 500 $\mu g{\cdot}mL^{-1}$. To understand the contribution from pure silica nanoparticles to bacterial inhibition, the bacterial growth influenced by S-SHSs, R-MSHSs-B and R-MSHSs at concentrations equal to that in nanoparticle/lysozyme formulations used in MIC assays was investigated. As shown in Figure S10, the bacterial toxicity follows the trend of SHSs > R-MSHSs-B > R-MSHSs at all lysozyme concentrations. This is because in one group, at a given lysozyme concentration, the dosage of three silica particles is different due to their large difference in lysozyme loading capacity. For example, at a lysozyme concentration of 100 $\mu g{\cdot}mL^{-1}$, the dosage of SHSs, R-MSHSs-B, and R-MSHSs is 1.64, 0.74, and 0.37 $mg{\cdot}mL^{-1}$, respectively. The large dosage difference explains the bacterial toxicity difference observed in Figure S10.

The trend in the antibacterial activity of lysozyme formulations (Figure 4c) is reversed compared to that of pure silica particles at all lysozyme concentrations under study (Figure S10). For instance, at the lysozyme concentration of 500 $\mu g{\cdot}mL^{-1}$, S-SHSs exhibit the highest toxicity (26%) but lowest antibacterial activity (76% in suppression) in the nano-lysozyme formulation. In contrast, R-MSHSs show the lowest bacterial toxicity (10%) contributed from particles themselves, but the highest bacterial inhibition (96%) is observed in the lysozyme−R-MSHSs formulation. This contrast suggests that the improved antibacterial performance is attributed to the sustained lysozyme release behavior and the enhanced adhesion performance of silica nanoparticles, rather than the nanoparticles themselves. Compared to S-SHSs, R-MSHSs-B with a sustained lysozyme release profile and enhanced adhesion toward bacteria are expected to achieve a higher antibacterial activity. Nevertheless, S-SHSs induce a higher bacterial toxicity (26%) than R-MSHSs-B (14%), leading to a comparable antibacterial activity (76%) between S-SHSs and R-MSHSs-B, as shown in Figure 4c.

To further demonstrate the advantage of silica nanopollens as lysozyme carriers, the long-term bacterial inhibition property was tested via bacteria kinetic tests under batch culture. As shown in the bacterial growth curve of *E. coli* without any treatment (Figure S11), the bacteria number experiences an exponential growth and keeps stationary within 3 days, then declines due to limited nutrition in the culture causing bacteria death. Therefore, the time-dependent bacterial growth at lysozyme concentration of 700 $\mu g{\cdot}mL^{-1}$ was monitored up to 3 days (Figure 4d). LB-agar plate assay (Figure 4d inset) was employed to examine the bacterial viability after the 3-day treatment. It can be observed that R-MSHSs maintained 100% bacterial inhibition throughout 3 days, which is the longest time

DOI: 10.1021/jacs.6b00243
J. Am. Chem. Soc. 2016, 138, 6455−6462

ever reported for full bacterial inhibition toward *E. coli* by using lysozyme.[21,24] This 3-day inhibition result is comparable to the performance of silver-loaded silica nanoparticles at 80 $\mu g \cdot mL^{-1}$, as demonstrated by the bacterial kinetic assay.[44] In contrast, time-dependent bacterial growth, as evidenced by the increased OD value, is observed in S-SHSs, R-MSHSs-B, and free lysozyme groups. No viable colonies can be observed on the agar plates for bacteria treated with lysozyme-R-MSHSs, showing the strong bactericidal activity of the silica nanopollens as opposed to the other samples (Figure 4d inset). The long-term bacterial inhibition property should be attributed to two advantages that originate in the design of silica nanopollens: (1) enhanced adhesion toward bacterial surface introduced by surface roughness, which results in efficient lysozyme delivery and enriched local concentration of lysozyme on bacterial surface, and (2) prolonged antimicrobial activity achieved by the sustained release of lysozyme from R-MSHSs, thus finally accelerating bacterial death via cell wall lysis and providing a continuous supply of active lysozyme to avoid regrowth of bacteria. However, due to the relatively weak particle−bacteria interaction and fast release profile, S-SHSs and R-MSHSs-B fail to inhibit the bacterial growth with inadequate lysozyme concentration delivered toward the bacterial surface.

To provide direct evidence on the bactericidal activity of lysozyme-loaded silica nanopollens, TEM and SEM were employed to observe the morphology of *E. coli* after 24 h treatment. Severe damage of the bacterial cell membrane can be clearly observed, enabling some of the silica nanopollens to sink into the cell (Figure 4e). Similarly, many semi-spherical dents can be observed on the bacterial surface from the SEM image (Figure 4f, indicated by white arrows), which may result from the detachment of lysozyme-loaded silica nanopollens from the bacteria surface during sample preparation. Both TEM and SEM observations indicate that even after lysozyme loading, silica nanopollens still maintain strong adhesion toward bacterial cell walls, leading to partial engulfment into the cell membrane. These results demonstrate efficient delivery of lysozyme to digest the bacterial cell wall, which is achieved through strong adhesion between the bacterial surface and the silica nanopollens.

Considering the complexity in a real biological environment, where a variety of proteins may coat on the nanoparticles' surfaces, forming protein corona and affecting their biological interactions and responses,[45−47] it is necessary to investigate the adhesion property and lysozyme delivery performance of silica nanopollens after they are coated by other proteins. Bovine serum albumin (BSA), as the most abundant serum representative protein (~50 $mg \cdot mL^{-1}$),[48] has been widely employed as a model for protein corona formation.[45,46] Here, both S-SHSs and R-MSHSs at 1 $mg \cdot mL^{-1}$ were incubated with BSA solution (50 $mg \cdot mL^{-1}$) at 37 °C for 2 h, after which a thick layer of BSA corona can be observed from the cryo-TEM image of S-SHSs (Figure 5a). In contrast, the surface roughness of R-MSHSs can still be recognized in Figure 5b after BSA coating, even though the space between surface silica spikes is almost filled with proteins. The bacteria adhesion property of S-SHSs and R-MSHSs was further investigated after BSA coating. The ICP results shown in Figure 5c indicate that the formation of BSA corona does not affect the adhesion of S-SHSs toward the bacterial surface with a silica amount of ~0.10 $pg \cdot cell^{-1}$, similar to the result in Figure 3d. For the silica nanopollens, less than 0.2 pg of R-MSHSs resides on each bacteria, which is lower compared with the bare nanoparticles (0.48 $pg \cdot cell^{-1}$).

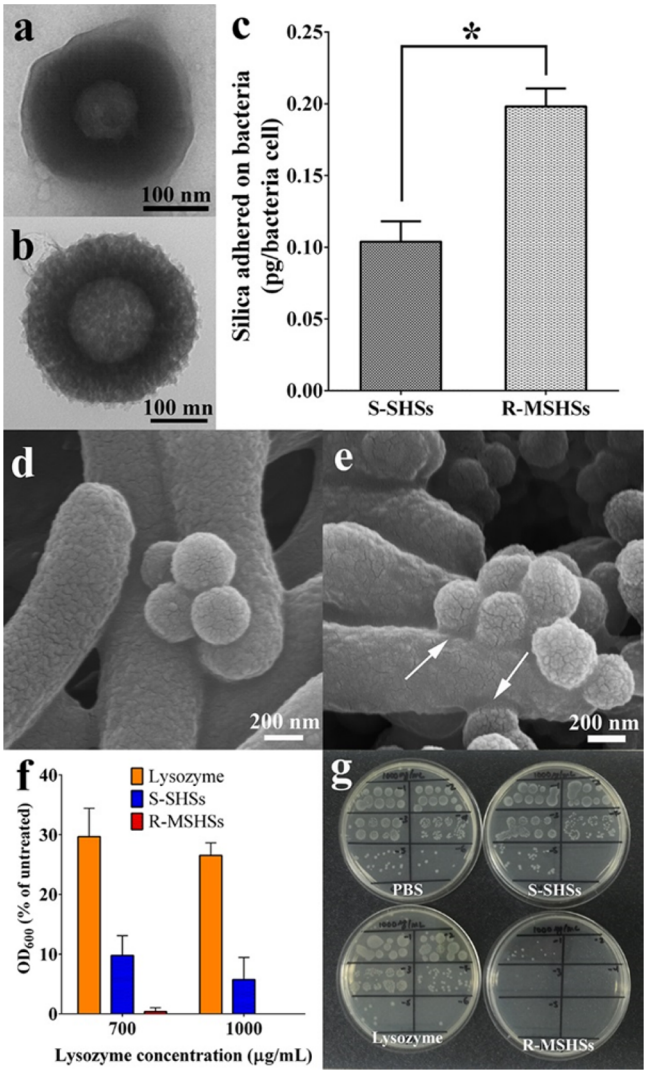

Figure 5. Cryo-TEM images of BSA-coated S-SHSs (a) and R-MSHSs (b), quantitative analysis of BSA-coated silica nanoparticles adhered on bacteria from ICP-OES (c) and their SEM images of S-SHSs (d) and R-MSHSs (e) adhered on *E. coli* surface, bacterial inhibition property of BSA-coated lysozyme−silica nanoparticles determined by OD@600 nm at lysozyme dosage of 700 and 1000 $\mu g \cdot mL^{-1}$ (f), and assessment of bacterial number via serial dilution spotting method at lysozyme dosage of 1000 $\mu g \cdot mL^{-1}$ (g).

This may be attributed to the decreased surface roughness after BSA coating. However, there is still a significant difference ($p < 0.05$) between smooth and rough nanoparticles toward bacteria adhesion. The interaction between silica nanoparticles and bacteria was further characterized using SEM, where particle partial engulfment can still be observed for R-MSHSs (white arrows in Figure 5e), indicating a relatively stronger particle−bacteria interaction as compared to S-SHSs (Figure 5d).

Upon the administration of lysozyme-loaded silica nanopollens into complex biological systems, the displacement of lysozyme by environmental molecules could be another concern.[49] To address this issue, silica nanoparticles loaded with lysozyme were further incubated in PBS solution with and without BSA, and the amounts of lysozyme leached were measured for comparison. As shown in Figure S12, around 43% of lysozyme leached out from S-SHSs in the presence of BSA, which is slightly higher than the amount released in the absence

DOI: 10.1021/jacs.6b00243
J. Am. Chem. Soc. 2016, 138, 6455−6462

of BSA (36%), indicating the environmental molecules promoted the release of lysozyme from S-SHSs. One possible reason is that lysozyme is coated on the outside of the particle's surface, which makes BSA displacement easy. In contrast, there is no obvious difference in lysozyme leaching for R-MSHSs with and without BSA (~21%), suggesting that the lysozyme loaded between the spikes is resistant to BSA displacement.

The antibacterial properties of lysozyme-loaded silica nanopollens after BSA coating were investigated at lysozyme concentrations of 700 and 1000 $\mu g \cdot mL^{-1}$. The MIC of lysozyme−silica nanopollen composites is 700 $\mu g \cdot mL^{-1}$ (Figure 4c); however, after BSA surface coating, the MIC increased to 1000 $\mu g \cdot mL^{-1}$ (Figure 5f). This may result from the impaired adhesion property of BSA-coated lysozyme−silica nanopollens, which slightly decreases the lysozyme delivery efficiency toward the bacterial surface for effective inhibition. As shown in Figure 5g, lysozyme-loaded silica nanopollens still exhibit potent bactericidal property even after BSA coating, with countable colony forming units (CFU) decreased from 10^6 to 10^2, much better than lysozyme, lysozyme-S-SHSs, and control groups.

To assess the antibacterial efficacy of lysozyme-loaded silica nanopollens in more realistic conditions, an *ex vivo* small-intestine infection model was built.[50,51] As illustrated in Figure 6a, fresh small-intestine segments (3 cm in length) were obtained from a healthy rat and pinned on an agarose gel layer with the luminal side facing up. A total of 5×10^6 CFU of ampicillin-resistant *E. coli* was introduced for small-intestine infection over 1 h, and then the tissues were transferred onto new plates with an agarose gel layer and cultured in DMEM/F-12 medium containing 5% fetal bovine serum. PBS, lysozyme, lysozyme−S-SHSs, and lysozyme−R-MSHSs were added into the medium at a lysozyme concentration of 5 $mg \cdot mL^{-1}$ for treatment over 24 h. The microbials on the tissue were carefully scraped and collected for CFU counting on ampicillin-containing agar plates via serial dilutions.[52] As can be clearly observed from Figure 6b, R-MSHSs exhibit a potent *ex vivo* antibacterial activity, with fewer colonies emerged as compared to PBS, lysozyme, and lysozyme−S-SHSs groups. Specifically, after treatment with lysozyme-loaded silica nanopollens, the *E. coli* count on small-intestine samples was lower by more than 2 orders of magnitude compared to the PBS and lysozyme-treated groups, and more than 30 times lower compared to lysozyme-loaded S-SHSs. The above results demonstrate that lysozyme-loaded silica nanopollens are efficient antibacterial agents and effectively inhibit bacterial survival both *in vitro* and *ex vivo*.

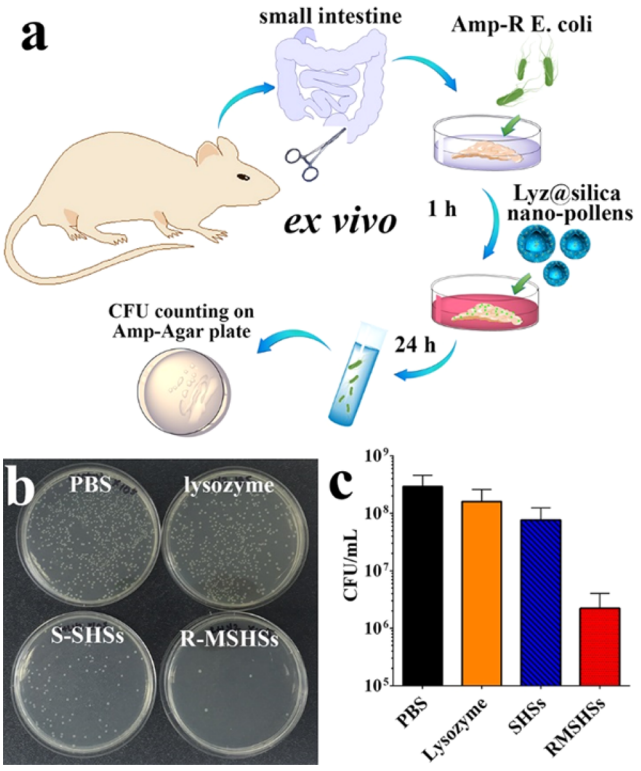

Figure 6. (a) Schematic illustration of the *ex vivo* antibacterial activity evaluation of lysozyme-loaded silica nanopollens. (b) Agar plates showing bacterial colonies in the small intestine after different treatment at $10^5\times$ dilution, and (c) corresponding surviving *E. coli* in the small intestine.

CONCLUSION

In summary, we have successfully prepared silica nanopollens through a one-pot, surfactant-free, cheap, and scalable approach. Because of their nanoscale surface roughness and accessible hollow cavities, silica nanopollens demonstrate enhanced adhesion toward bacterial surfaces and sustained release of lysozyme, which promote lysozyme enrichment on bacterial surfaces. This silica nanopollens-based lysozyme formulation exhibits potent antibacterial activity and a prolonged bacterial inhibition up to 3 days toward *E. coli*. The bacteria adhesion property of silica nanopollens can be maintained after surface protein coating, achieving an excellent antimicrobial activity of lysozyme-loaded silica nanopollens both *in vitro* and *ex vivo*. This work provides a nature-inspired concept for the rational design of nanocarriers with high performance in widespread drug delivery applications.

ASSOCIATED CONTENT

Supporting Information

The Supporting Information is available free of charge on the ACS Publications website at DOI: 10.1021/jacs.6b00243.

Experimental details and characterization data, including Figures S1−S12 and Tables S1 and S2 (PDF)
Electron tomography movie (AVI)

AUTHOR INFORMATION

Corresponding Author

*c.yu@uq.edu.au

Notes

The authors declare no competing financial interest.

ACKNOWLEDGMENTS

The authors acknowledge support from the Australian Research Council, Queensland Government, the Australian National Fabrication Facility, and the Australian Microscopy and Microanalysis Research Facility at the Centre for Microscopy and Microanalysis, University of Queensland.

REFERENCES

(1) Feng, L.; Li, S.; Li, Y.; Li, H.; Zhang, L.; Zhai, J.; Song, Y.; Liu, B.; Jiang, L.; Zhu, D. *Adv. Mater.* **2002**, *14*, 1857.
(2) Wegst, U. G. K.; Bai, H.; Saiz, E.; Tomsia, A. P.; Ritchie, R. O. *Nat. Mater.* **2015**, *14*, 23.
(3) Kong, B.; Tang, J.; Wu, Z.; Selomulya, C.; Wang, H.; Wei, J.; Wang, Y.; Zheng, G.; Zhao, D. *NPG Asia Mater.* **2014**, *6*, e117.

DOI: 10.1021/jacs.6b00243
J. Am. Chem. Soc. 2016, 138, 6455−6462

(4) Feng, J.; Lin, L.; Chen, P.; Hua, W.; Sun, Q.; Ao, Z.; Liu, D.; Jiang, L.; Wang, S.; Han, D. *ACS Appl. Mater. Interfaces* **2015**, *7*, 8961.
(5) Barrier, S.; Diego-Taboada, A.; Thomasson, M. J.; Madden, L.; Pointon, J. C.; Wadhawan, J. D.; Beckett, S. T.; Atkin, S. L.; Mackenzie, G. *J. Mater. Chem.* **2011**, *21*, 975.
(6) Edlund, A. F.; Swanson, R.; Preuss, D. *Plant Cell* **2004**, *16*, S84.
(7) Thorp, R. W. *Plant Syst. Evol.* **2000**, *222*, 211.
(8) Zhu, P.; Liu, J.; Bess, J.; Chertova, E.; Lifson, J. D.; Grisé, H.; Ofek, G. A.; Taylor, K. A.; Roux, K. H. *Nature* **2006**, *441*, 847.
(9) Sougrat, R.; Bartesaghi, A.; Lifson, J. D.; Bennett, A. E.; Bess, J. W.; Zabransky, D. J.; Subramaniam, S. *PLoS Pathog.* **2007**, *3*, e63.
(10) Fasting, C.; Schalley, C. A.; Weber, M.; Seitz, O.; Hecht, S.; Koksch, B.; Dernedde, J.; Graf, C.; Knapp, E.-W.; Haag, R. *Angew. Chem., Int. Ed.* **2012**, *51*, 10472.
(11) Xia, F.; Jiang, L. *Adv. Mater.* **2008**, *20*, 2842.
(12) Yoo, J.-W.; Irvine, D. J.; Discher, D. E.; Mitragotri, S. *Nat. Rev. Drug Discovery* **2011**, *10*, 521.
(13) Ahmad Nor, Y.; Niu, Y.; Karmakar, S.; Zhou, L.; Xu, C.; Zhang, J.; Zhang, H.; Yu, M.; Mahony, D.; Mitter, N.; Cooper, M. A.; Yu, C. *ACS Cent. Sci.* **2015**, *1*, 328.
(14) Niu, Y.; Yu, M.; Hartono, S. B.; Yang, J.; Xu, H.; Zhang, H.; Zhang, J.; Zou, J.; Dexter, A.; Gu, W.; Yu, C. *Adv. Mater.* **2013**, *25*, 6233.
(15) Fischbach, M. A.; Walsh, C. T. *Science* **2009**, *325*, 1089.
(16) Neu, H. C. *Science* **1992**, *257*, 1064.
(17) Chipman, D. M.; Sharon, N. *Science* **1969**, *165*, 454.
(18) Masschalck, B.; Michiels, C. W. *Crit. Rev. Microbiol.* **2003**, *29*, 191.
(19) Kiristi, M.; Singh, V. V.; Esteban-Fernández de Ávila, B.; Uygun, M.; Soto, F.; Aktaş Uygun, D.; Wang, J. *ACS Nano* **2015**, *9*, 9252.
(20) James, S.; McManus, J. *J. Phys. Chem. B* **2012**, *116*, 10182.
(21) Tripathy, N.; Ahmad, R.; Bang, S. H.; Min, J.; Hahn, Y.-B. *Chem. Commun.* **2014**, *50*, 9298.
(22) Rubin, J.; San Miguel, A.; Bommarius, A. S.; Behrens, S. H. *J. Phys. Chem. B* **2010**, *114*, 4383.
(23) Pavlukhina, S.; Lu, Y.; Patimetha, A.; Libera, M.; Sukhishvili, S. *Biomacromolecules* **2010**, *11*, 3448.
(24) Li, L. L.; Wang, H. *Adv. Healthcare Mater.* **2013**, *2*, 1351.
(25) Franca de Oliveira, L.; de Almeida Goncalves, K.; Boreli, F. H.; Kobarg, J.; Cardoso, M. B. *J. Mater. Chem.* **2012**, *22*, 22851.
(26) Bhattacharyya, M. S.; Hiwale, P.; Piras, M.; Medda, L.; Steri, D.; Piludu, M.; Salis, A.; Monduzzi, M. *J. Phys. Chem. C* **2010**, *114*, 19928.
(27) Kao, K.-C.; Lin, T.-S.; Mou, C.-Y. *J. Phys. Chem. C* **2014**, *118*, 6734.
(28) Luckarift, H. R.; Dickerson, M. B.; Sandhage, K. H.; Spain, J. C. *Small* **2006**, *2*, 640.
(29) Craig, L.; Pique, M. E.; Tainer, J. A. *Nat. Rev. Microbiol.* **2004**, *2*, 363.
(30) Chen, M.; Yu, Q.; Sun, H. *Int. J. Mol. Sci.* **2013**, *14*, 18488.
(31) Ivanova, E. P.; Truong, V. K.; Wang, J. Y.; Berndt, C. C.; Jones, R. T.; Yusuf, I. I.; Peake, I.; Schmidt, H. W.; Fluke, C.; Barnes, D.; Crawford, R. J. *Langmuir* **2010**, *26*, 1973.
(32) Truong, V. K.; Lapovok, R.; Estrin, Y. S.; Rundell, S.; Wang, J. Y.; Fluke, C. J.; Crawford, R. J.; Ivanova, E. P. *Biomaterials* **2010**, *31*, 3674.
(33) Wu, X.; Tian, Y.; Cui, Y.; Wei, L.; Wang, Q.; Chen, Y. *J. Phys. Chem. C* **2007**, *111*, 9704.
(34) Brandon Goodwin, W.; Gomez, I. J.; Fang, Y.; Meredith, J. C.; Sandhage, K. H. *Chem. Mater.* **2013**, *25*, 4529.
(35) Tolnai, G.; Csempesz, F.; Kabai-Faix, M.; Kálmán, E.; Keresztes, Z.; Kovács, A. L.; Ramsden, J. J.; Hórvölgyi, Z. *Langmuir* **2001**, *17*, 2683.
(36) Friedrich, H.; de Jongh, P. E.; Verkleij, A. J.; de Jong, K. P. *Chem. Rev.* **2009**, *109*, 1613.
(37) Yuan, P.; Liu, N.; Zhao, L.; Zhou, X.; Zhou, L.; Auchterlonie, G. J.; Yao, X.; Drennan, J.; Lu, G. Q.; Zou, J.; Yu, C. *Angew. Chem., Int. Ed.* **2008**, *47*, 6670.
(38) Liu, J.; Qiao, S. Z.; Liu, H.; Chen, J.; Orpe, A.; Zhao, D.; Lu, G. Q. *Angew. Chem., Int. Ed.* **2011**, *50*, 5947.
(39) Zhang, H.; Yu, M.; Song, H.; Noonan, O.; Zhang, J.; Yang, Y.; Zhou, L.; Yu, C. *Chem. Mater.* **2015**, *27*, 6297.
(40) Agudo-Canalejo, J.; Lipowsky, R. *ACS Nano* **2015**, *9*, 3704.
(41) Mo, Y.; Turner, K. T.; Szlufarska, I. *Nature* **2009**, *457*, 1116.
(42) Kim, J. A.; Åberg, C.; de Cárcer, G.; Malumbres, M.; Salvati, A.; Dawson, K. A. *ACS Nano* **2013**, *7*, 7483.
(43) Vinu, A.; Murugesan, V.; Hartmann, M. *J. Phys. Chem. B* **2004**, *108*, 7323.
(44) Tian, Y.; Qi, J.; Zhang, W.; Cai, Q.; Jiang, X. *ACS Appl. Mater. Interfaces* **2014**, *6*, 12038.
(45) Fleischer, C. C.; Payne, C. K. *Acc. Chem. Res.* **2014**, *47*, 2651.
(46) Wang, L.; Li, J.; Pan, J.; Jiang, X.; Ji, Y.; Li, Y.; Qu, Y.; Zhao, Y.; Wu, X.; Chen, C. *J. Am. Chem. Soc.* **2013**, *135*, 17359.
(47) Lesniak, A.; Salvati, A.; Santos-Martinez, M. J.; Radomski, M. W.; Dawson, K. A.; Åberg, C. *J. Am. Chem. Soc.* **2013**, *135*, 1438.
(48) Imbert-Bismut, F.; Ratziu, V.; Pieroni, L.; Charlotte, F.; Benhamou, Y.; Poynard, T. *Lancet* **2001**, *357*, 1069.
(49) Monopoli, M. P.; Walczyk, D.; Campbell, A.; Elia, G.; Lynch, I.; Baldelli Bombelli, F.; Dawson, K. A. *J. Am. Chem. Soc.* **2011**, *133*, 2525.
(50) Bansal, D.; Ave, P.; Kerneis, S.; Frileux, P.; Boché, O.; Baglin, A. C.; Dubost, G.; Leguern, A.-S.; Prevost, M.-C.; Bracha, R.; Mirelman, D.; Guillén, N.; Labruyère, E. *PLoS Neglected Trop. Dis.* **2009**, *3*, e551.
(51) de Graaf, I. A. M.; Olinga, P.; de Jager, M. H.; Merema, M. T.; de Kanter, R.; van de Kerkhof, E. G.; Groothuis, G. M. M. *Nat. Protoc.* **2010**, *5*, 1540.
(52) Thomas, P.; Sekhar, A. C.; Upreti, R.; Mujawar, M. M.; Pasha, S. S. *Biotechnol. Rep.* **2015**, *8*, 45.

DOI: 10.1021/jacs.6b00243
J. Am. Chem. Soc. 2016, 138, 6455−6462